

Observation of changes in the atomic and electronic structure of single-crystal $\text{YBa}_2\text{Cu}_3\text{O}_{6.6}$ accompanying bromination

L. M. Dieng,¹ A. Yu. Ignatov,¹ T. A. Tyson,¹ M. Croft,² F. Dogan,³ C.-Y. Kim,⁴ J. C. Woicik,⁵ and J. Grow⁶¹*Department of Physics, New Jersey Institute of Technology, Newark, New Jersey 07102*²*Department of Physics and Astronomy, Rutgers University, Piscataway, New Jersey 08854**and National Synchrotron Light Source, Brookhaven National Laboratory, Upton, New York 11973*³*Department of Materials Science and Engineering, University of Washington, Seattle, Washington 98195*⁴*Bell Laboratories, Lucent Technologies, Murray Hill, New Jersey 07974*⁵*National Institute of Standards and Technology, Gaithersburg, Maryland 20899*⁶*Department of Chemistry and Chemical Engineering, New Jersey Institute of Technology, Newark, New Jersey 07102*

(Received 8 January 2001; revised manuscript received 18 January 2002; published 26 June 2002)

To ascertain the role of bromination in the recovery of superconductivity in underdoped $\text{YBa}_2\text{Cu}_3\text{O}_{6+y}$ (YBCO), we have performed polarized multiple-edge x-ray-absorption fine structure (XAFS) measurements on normal ($y \sim 0.6$) and brominated ($\text{Br}/\text{Cu} \sim 1/30$, $y \sim 0.6$) single crystals with superconducting transitions at 63 and 89 K, respectively. The brominated sample becomes strongly heterogeneous on an atomic length scale. Approximately one-third of YBCO is locally decomposed yet incorporated as a well-ordered “host” lattice as nanoscale regions. The decomposed phase consists of heavily distorted domains with an order not following that of the “host” lattice. Structurally, these domains are fragments of the YBCO lattice that are discontinued along the Cu(1)-O(1) containing planes. The local structure is consistent with the cluster expansions: $\text{Y-O}(2,3)_8\text{-Cu}(2)_8\text{-}\dots$, $\text{Ba-O}_8\text{-Cu}(2)_4\text{Cu}(1)_2\text{-}\dots$, and $\text{Cu-O}_4\text{-}\dots$ about the Y, Ba, and Cu sites. Interatomic distances and Debye-Waller factors for the expansions were determined from fits to Y K -, Ba L_{3-} , and Cu K -edge XAFS data at room temperature. Br K -edge data reveal that Br does not enter substitutionally or interstitially into the *perfect* YBCO lattice. However, Br does occupy the Cu(1) sites in a nanofragment of the YBCO lattice, forming Br-O(4)-Ba-Cu₂(1)Cu(2)-... nanoclusters. From polarized measurements these nanoclusters were found to be almost randomly oriented with respect to the “host” crystal, and probably are the nucleus of the decomposed phase. This heterogeneity brings about the unusual structural and electronic properties of the normal state previously reported in the literature. Implications on for diffraction, transport, and magnetization measurements are discussed.

DOI: 10.1103/PhysRevB.66.014508

PACS number(s): 74.72.Bk, 61.10.Ht, 78.70.Dm, 74.62.Dh

I. INTRODUCTION

The recovery of superconductivity in underdoped $\text{YBa}_2\text{Cu}_3\text{O}_{6+y}$ (YBCO) by exposure to bromine is a long-standing problem which has not been clearly resolved. The key question concerns the role of Br in the lattice. Whether Br is incorporated into one of the crystallographic sites and dopes the system¹⁻³ or if it causes a local decomposition reaction to occur, creating an amorphous products, liberating oxygen, and oxygenating the underdoped unreacted regions,⁴ remains in dispute.

The first observation of the effect was made by Osipyan *et al.*,¹ who reported a critical temperature (T_c) of 90–92 K and an orthorhombic phase formed by exposing initially tetragonal, $y \sim 0$, YBCO samples to gaseous chlorine.^{1(a)} Further work by this group showed that exposure to Br_2 and I_2 resulted in the recovery of superconductivity^{1(b)} with $T_c = 80\text{--}85$ and 55 K, respectively. Radousky *et al.*² performed systematic structural (x-ray diffraction), spectroscopic, and analytic measurements in an attempt to ascertain the role of Br in the restoration of superconductivity. In x-ray-diffraction (XRD) measurements, bromination was found to increase peak widths and to introduce a diffuse background typical of a partly amorphous phases. The diffraction pattern was not significantly different from the oxygen-rich ortho-

rhombic YBCO pattern. Bromination was found to alter significantly the Raman-active phonons, changing the O(4) (Ref. 5) vibration frequencies. These experiments, however, were not able to ascertain the location and chemistry of the Br atoms.

X-ray photoelectron spectra of brominated YBCO suggested that Br could have a chemical environment similar to that in BaBr_2 .⁶ Several bulk-sensitive measurements attempted to resolve the structural changes induced by bromination of underdoped YBCO. Neutron-diffraction studies suggested that Br occupies vacant O(1) sites.⁷ Earlier x-ray-absorption fine-structure (XAFS) measurements at the Y K edge⁸ found no changes in the local structure about the Y sites, while it was claimed, from the Br K -edge data, that Br entered vacancies in planes containing Cu(1)-O(1). Recently, Potrepka *et al.*⁹ investigated the local atomic structure (about Cu and Br) using ^{63,65}Cu nuclear quadrupole resonance and ^{79,81}Br nuclear magnetic resonance (NMR) on well-characterized powder samples of parent, deoxygenated, and brominated YBCO. The NMR signal for the Cu(2) peak in brominated samples was found to be broadened compared to that in the parent materials. This was interpreted as proof of the possible coexistence of a broad contribution from a component where the Cu(2) near-neighbor environment had been perturbed and has a sharp contribution reminiscent of Cu(2)

sites in a well-ordered superconductor (two-phase model). However, neither the phase ratio nor the details of the local structure of the perturbed phase were determined. Potrepka *et al.* also performed low-temperature Br *K*-edge XAFS measurements,⁹ and argued that Br did not enter the lattice substitutionally or interstitially. XAFS spectra were found to be similar to those of BaBr₂ powder. They suggested that bromination led to BaBr₂ precipitation as nanoparticles which gave rise to the higher background seen in XRD. Unfortunately, a model fitting of the XAFS spectrum was not performed, and hence the details of local structure about Br remained unknown.

The motivation of this paper is to provide a quantitative characterization of local distortions about Br, Cu, Ba, and Y sites (leading to a three-dimensional picture) and to determine the location of the Br atoms and possible phase composition of the brominated YBa₂Cu₃O_{6+y} ($y \sim 0.6$) crystal. In contrast to previous XAFS measurements, we utilized slightly brominated crystals (one Br atom per 30 Cu atoms; see Sec. II) combined with x-ray fluorescence yield (FY) measurements. Use of well-oriented samples was important because it allows one to take advantage of the high degree of linear polarization of synchrotron x rays to isolate the atomic species contributing to the XAFS signal. For instance, *c*-axis-polarized XAFS provides a direct probe of Cu(1)-O(4) and Cu(2)-O(4) pairs, eliminating contributions from the “in-plane” Cu(2)-O(2,3) pairs and, therefore, reduces the number of parameters in the XAFS fit. The number of free parameters is sufficient to perform a quantitative characterization of *two phases*, enabling us to address the issue of possible phase separation in brominated YBCO. FY measurements do not require a high Br content. Moreover, slightly brominated samples appear to be less structurally distorted and less subjected to possible decomposition reactions,⁴ simplifying the structural analysis while keeping the physics unchanged.

The combined analysis of the Cu *K*-, Ba *L*₃-, and Y *K*-edge XAFS data undertaken in this work has a significant advantage over traditional single-edge XAFS. In distorted multiple-phase compounds the probing length of XAFS is typically limited to 3–4 Å (2–3 first coordination shells about the absorption site). In order to determine what part of the YBCO unit is affected by bromination, the local distortions introduced about the Cu, Ba, and Y sites must be compared.

In Sec. II, we describe experimental details and data analysis for mixed-phase compounds. In Sec. III A, Br *K*-edge XAFS analysis will be used to show that *Br does not enter a perfect YBCO lattice*, while it does occupy the Cu(1) position in fragment of the lattice forming a nano-cluster of Br-O(4)-Ba-Cu(1)Cu(2)-.... *c*-axis-polarized Cu *K*-edge XAFS reveals that the Cu-O pair distribution of the brominated sample can be best described in terms of a two-phase model with a 2:1 ratio of Cu(1,2)-O(4) pairs [as in the well-ordered YBCO ($y \sim 0.9-1$)] and presumably Cu(2)-O(2,3) pairs of ~ 1.95 Å (Sec. III B). This result is further supported by polarized Cu *K*-edge x-ray-absorption near-edge structure (XANES) measurements given in Sec. III C. The behavior of major peaks in the XANES spectra suggest a reoxygenation

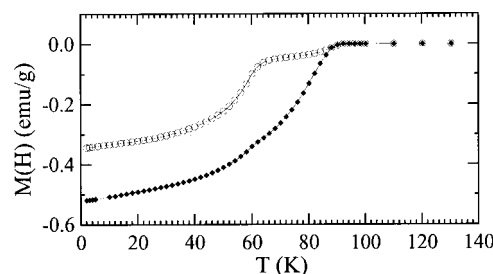


FIG. 1. Zero-field-cooled magnetization vs temperature in a 20-Oe magnetic field for brominated (diamonds) and normal (open circles) YBCO ($y \sim 0.6$). Spectra are not corrected for the demagnetization factor. T_c is taken at the onset for superconductivity. The untreated sample has a minor component ($\sim 15\%$) with $T_c \sim 88$ K, and major component with $T_c \sim 63$ K. Bromination produces samples with $T_c \sim 89$ K.

of about two-thirds of the brominated sample accompanied by the appearance of a decomposed phase exhibiting a weak polarization dependence. Ba *L*₃-edge and Y *K*-edge XAFS are presented in Secs. III D and III E. A multiple-edge data analysis outlined in Sec. IV is consistent with the formation of a strongly heterogeneous sample as a result of bromination. About one third of the YBCO is decomposed. This decomposed phase consists of nanodomains of the fragmented YBCO lattice which are embedded in a “host” lattice resembling well-ordered oxygen-rich YBa₂Cu₃O_{6+y} ($y \sim 0.9-1$). The fragmentation takes place mostly along the planes containing Cu(1)-O(1) accompanied by a rearrangement of the nanodomains. The implications of diffraction, magnetization, and resistivity measurements are discussed at the end of Sec. IV, and the conclusions of this work are summarized in Sec. V.

II. EXPERIMENTAL DETAILS AND DATA REDUCTION

Single crystals of YBa₂Cu₃O_{6+y} ($y \sim 0.6$) were prepared for the experiments conducted. YBa₂Cu₃O_{6+y} powders doped with Y₂BaCuO₅ and Pt were compacted by pressing. A seed crystal of SmBa₂Cu₃O₇ was placed on the top center of this compact. The sample was heated to 1050 °C and cooled below the peritectic melting temperature. The nucleation and growth process of undercooled semisolid YBCO was initiated by the seed crystal at 1005 °C. The YBCO crystal was then grown under isothermal conditions. Samples for XAFS studies were prepared by cleaving of the crystals along the *ab* plane.

A pair of single crystals from the same batch (with the same oxygen content) was used in these experiments. One YBCO crystal was brominated by exposing it to Br₂ vapor in a nitrogen atmosphere at 260 °C for 1 h in a tube furnace. The bromine content was determined by QTI Inc. using a combustion and titration techniques and was found to be about 1.25-wt%—corresponding to a Br:Cu ratio of $\sim 1:30$. Zero-field-cooled magnetization measurements (in a 20-Oe magnetic field) on the brominated sample were compared with those of normal crystal (Fig. 1), revealing an enhancement of the critical temperature from 63 to 89 K. Synchrotron high-resolution XRD data were collected at beam line

X16B of the National Synchrotron Light Source (NSLS). The diffraction patterns revealed no evidence for secondary crystallographic phases.

XAFS data were collected at NSLS beamlines X23A2 [Cu K -edge Si(311) monochromator], X19A [Ba L_3 -edge Si(111) monochromator], X18B [Br K -edge Si(111) monochromator], and X11A [Y K -edge Si(111) monochromator] in FY mode at room temperature. Special care was taken to suppress higher-order x-ray harmonics. We used a passivated implanted planar silicon (PIPS) detector and a $Z-1$ filter to obtain the total FY at Cu K , Ba L_3 , and Y K edges and a 13-element Ge detector with an energy resolution of 260 eV to detect the partial $K\alpha$ yield at the Br K -edge. The absolute energy scales were calibrated by a standard procedure,¹⁰ using a set of pure metal foils: Cu, Ti, Y, and Pt for Cu K -, Ba L_3 -, Y K -, and Br K -edge data, respectively. The reproducibility of the Cu K - and Br K -edge XANES spectra was achieved through repeated measurements of the studied samples. From 2 to 12 scans (at the Br K edge) were collected to improve the signal-to-noise ratios.

For Cu K -edge XAFS measurements the single crystals were aligned so that an angle between the polarization vector of oncoming x rays, \mathbf{E} , and the surface normal (which coincides with the c axis) was $\varphi \sim 20 \pm 5^\circ$, giving predominantly the $\mathbf{E} \parallel \mathbf{c}$ spectrum. For the Ba L_3 and Y K edges we used $\varphi \sim 90 \pm 5^\circ$, yielding $\mathbf{E} \parallel \mathbf{ab}$ spectra. The PIPS detector was placed at $\phi \sim 60^\circ$ with respect to the direction of the oncoming x-rays. Br K -edge measurements were performed at $\varphi \sim 45 \pm 5^\circ$, with the Ge detector positioned at $\phi \sim 90^\circ$. For the above experimental conditions, the sampling depths (x-ray penetration depth) (Ref. 11) were estimated to be $\sim 2000 \text{ \AA}$ for the Cu K edge, $\sim 1400 \text{ \AA}$ for the Ba L_3 edge, and more than 3000 \AA for Y K - and Br K edges, yielding XAFS measurements that are bulk sensitive. Further measurements at different grazing angles of the oncoming x-ray beam must be done to address the depth dependence of the bromination.

All spectra except the Br K -edge XAFS data were corrected for self-absorption using the atomic absorption coefficients from Ref. 12. We further accounted for the large solid angle of the PIPS detector and for contributions from both Cu K_α and K_β lines. Reduced Cu K -edge $k\chi(k)$ and Br K -edge $k\chi(k)$ are shown in Fig. 2. Cu K -edge spectra were limited in k space due to Bragg reflections. Ba L_3 -edge data were cut off by the Ba L_2 edge at $\sim 9.5 \text{ \AA}^{-1}$. Upper limits for Br K - and Y K -edge XAFS spectra (~ 11.5 and 15 \AA^{-1}) were based on the signal-to-noise ratios in the raw data.

Data analysis was performed according to standard procedures.¹⁰ Usually an XAFS analysis is performed on single-phase materials that are checked by x-ray diffraction and/or EDAX measurements. In brominated YBCO, a mixture of phases some of which are possibly amorphous have been discussed in the literature.^{4,9} Therefore, before going into a detailed analysis, we briefly examine the XAFS for a mixture of m different phases. Assuming that the typical size of a nanoparticle is larger than $5\text{--}6 \text{ \AA}$ (that is the approximate cutoff limit of x-ray absorption spectroscopy) an effective coordination number is given by $N_{\text{eff}} = 3N_j p_m \cos^2(\theta_j)$, where N_j atoms at distances R_j , and p_m is a partial weight of the m th nanoparticle which follows the normalization rule:

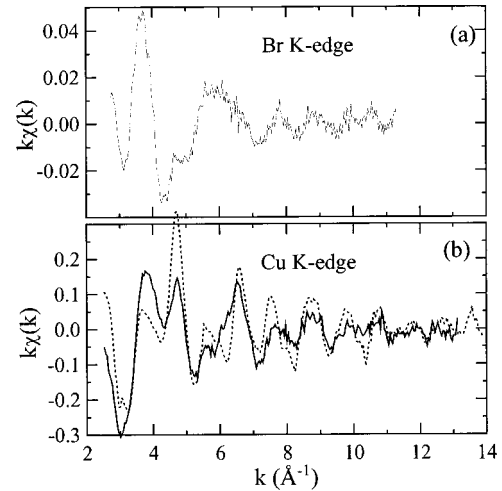


FIG. 2. (a) Br K -edge $k\chi(k)$ vs k for brominated YBCO with an x-ray polarization at 45° to the c axis. (b) Cu K -edge $k\chi(k)$ vs k for brominated (solid line) and pristine YBCO ($y \sim 0.6$) (dashed line) with an x-ray polarization parallel to the c axis. Cu K -edge data were corrected for self-absorption as described in Ref. 11.

$\sum p_m = 1$. θ denotes the angle between the polarization vector of an oncoming x ray and the unit vector pointing along the direction from the absorbing atom to the scattering atom. The structural parameters R_j , N_j , and σ_j^2 (Debye-Waller factor) become phase dependent. The phase sensitivity p_m is limited by the typical error in determining N_{eff} ($10\text{--}20\%$). Since Br in Br-YBCO is at the level of an impurity (1 Br per 30 Cu), neither the Cu K , Ba L_3 or Y K -edge XAFS measurements have the potential to determine the Br location with respect to the Cu, Ba, and Y sites.

Instead, Cu K -, Ba L_3 -, and Y K -edge XAFS will be used to obtain information on the local structure of the *major phase(s)* created by bromination. Usually, the number of structural parameters available in the fit¹³ allows one to consider a mixture of no more than two phases. This simple model, however, appears to satisfy the results of the important experimental observations.⁴ One of the phases is associated with the parent YBCO, which might have a slightly modified local structure and oxygen stoichiometry. Another phase accounts for locally decomposed regions (domains) characterized by a possible nonstoichiometric composition and low dimensionality (large local distortions). We shall further discuss the validity of the two-phase approximation (Sec. IV), invoking results of our multiple-edge XAFS analysis. The local structure of specific atomic sites will be expressed in terms of cluster expansions including the first oxygen shell about Cu(1,2) (Sec. III B) and the first two shells about Ba and Y (Secs. III D and III E).

Photoelectron backscattering amplitudes and total phase shifts required to perform the fits¹⁰ were generated by the FEFF-6 code¹⁴ using clusters with a radius $\sim 8 \text{ \AA}$ around the Cu(1,2), Ba, and Y absorption sites. The clusters were constructed using the neutron-diffraction data of YBCO ($y = 0.51$).¹⁵ Incorporated Br was ignored, since it was at the level of an impurity. For the decomposed phase we used the same amplitudes and phase shifts as for pristine YBCO. This *ad hoc* approximation will be verified in Secs. III B, III D, and III E. This is expected to be satisfactory provided that the

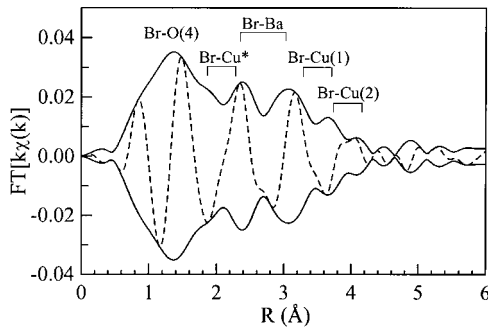


FIG. 3. The Fourier transform (FT) of brominated YBCO. The oscillating curve (dashed line) is the imaginary part of the FT. The envelope (solid curve) is the magnitude of the FT. The data are transformed with a square window between 2.9 and 11.4 \AA^{-1} . The peak assignment is based on the multiple-shell model described in Sec. III A. $k\chi(k)$ for this model is shown in Fig. 4.

decomposed phase mostly consists of nanofragments of an YBCO lattice where the average interatomic distances and the three-dimensional arrangement of atoms are similar to those in YBCO, while the coordination numbers could be different. For the Br K -edge analysis, the amplitudes and phase shifts were initially determined by the FEFF-3 code utilizing atomic potentials. As the location of Br was determined in a first approximation, a cluster about Br atom was assembled and more accurate amplitude and phase shifts were generated by FEFF-6.

III. EXPERIMENTAL RESULTS

A. Br K edge

The Br K -edge spectrum shown in Fig. 2(a) was Fourier transformed to r space over a range of 2.9–11.4 \AA using a square window. The resulting magnitude and imaginary parts are plotted in Fig. 3. Although the peak heights are relatively small, the multiple-shell structure about Br is apparent from the plot.

The complex structure of the Br K -edge analysis comes from the fact that neither the chemical composition nor the local structure of Br atoms are known *a priori*. In an attempt to refine the structure we will proceed in several steps, narrowing the choice for possible structural models and finally discussing the uniqueness of the fit. As a first step, we estimate contribution from Br-X pair(s) through a back Fourier transformation over the range 0.7–1.7 \AA . Although the first peak is not perfectly separated from the others, filtered XAFS enables the chemical composition and quantitative structural parameters of the Br nearest neighbor to be determined. It should be mentioned that the peak at ~ 1.5 \AA usually corresponds to the oxygen coordination. Bromine-to-metal bonds are characterized by larger interatomic distances. Nevertheless, all four elements constituting YBCO were considered. Results of a direct XAFS simulation over the range 4–10.5 \AA showed that the first peak, indeed, corresponded to a Br-O pair, while neither metals or mixtures of metals could fit the data. The best fit reveals a Br-O interatomic distance $R = 1.83 \pm 0.02$ \AA , a Debye-Waller factor $\sigma^{(2)} = 0.013 \pm 0.003$ \AA^2 , and a coordination number $N = 0.9$

± 0.3 . Note that the extracted Br-O distance coincides with the Cu(1)-O(4) distance in YBCO. This prompted us to check the hypothesis that Br enters the Cu(1) site of oxygen-deficient YBCO ($y \rightarrow 0$). In order to show that Br-O distribution has no peak at about 1.93 \AA [that corresponds to the Cu(1)-O(1) bond in oxygen-rich YBCO], a two-site distribution peaking at 1.83 and 1.93 \AA was attempted. This two-peak fit collapses to a single-site distribution at about 1.83 \AA . In normal YBCO all Cu(1) sites are occupied (the on-site deficiency appears to be well below of the amount of Br introduced in the sample). Therefore, in the framework of our hypothesis, for substituted Br atoms there is one Cu atom removed which is potentially available to be bonded to the liberated oxygen (Sec. III B) or bromine. The latter will be considered in a form of a “nanocopper bromide” (referred to below as CuBr*), with local structural parameters (Br-Cu interatomic distance, DW factor, and coordination number) to be determined along with the structural parameters of the phase with Br in the Cu(1) position. Its worth mentioning that though our synchrotron x-ray-diffraction data ruled out the presence of CuBr in our crystal compared to previous work, which reported traces of CuBr.¹⁶ Thus we considered CuBr* along with a phase with Br in the Cu(1) position. If the amount of CuBr* in brominated crystal is negligible, then the Br-Cu coordination number should approach zero.

The Fourier-transformed $k\chi(k)$ data were back transformed from 0.7 to 4.26 \AA . The resulting XAFS was fit in the single-scattering approximation¹⁷ assuming Br-O(4), Br-Ba, Br-Cu(1), and Br-Cu(2) peaks at 1.83, 2.51, 3.87, and 4.19 \AA for the phase with Br in the Cu(1) position, and a Br-Cu peak at 2.42 \AA for the CuBr* phase. For the fitting range from 3.7 to 11.3 \AA^{-1} the maximum allowed number of varying parameters is 18.¹³ We performed a constrained fit using 14 free parameters: The energy shift for the Br-O shell and S_o^2 factors for all shells were fixed as estimated from the first peak fit described above. In addition, we constrained all coordination numbers in order to determine the shape of clusters about Br atoms. For instance, if Br is in the Cu(1) position of an oxygen-deficient YBCO lattice, it has to be twofold coordinated to O(4), eightfold coordinates to Ba, fourfold coordinates to Cu(1), and twofold coordinates to Cu(2). Taking into account the experimental geometry of our polarized Br K -edge measurements (Sec. II), the effective coordination numbers should be 3, 5.9, 3, and 3, respectively. If the top four of eight unit cells are missing (as a result of decomposition reaction occurring upon bromination) the expected effective coordination numbers should be half of those listed above. Clusters of other shapes which are a fraction of the well-aligned “host” lattice can be considered accordingly. We also expanded the search to clusters, which are randomly oriented with respect to the host single-crystal structure. We found that, to obtain a reasonable fit, the Br-Ba coordination number should not exceed $\frac{3}{2}$, thereby limiting the number of aligned cells to two units and suggesting an open structure with Br on its surface. If two units are connected along the c axis or either a or b axes, then the O(4) coordination number should be 3 or $\frac{3}{2}$ —both fall beyond the oxygen coordination of 0.9 ± 0.3 estimated from the first peak fit. The experimental data are better fit with one atom of

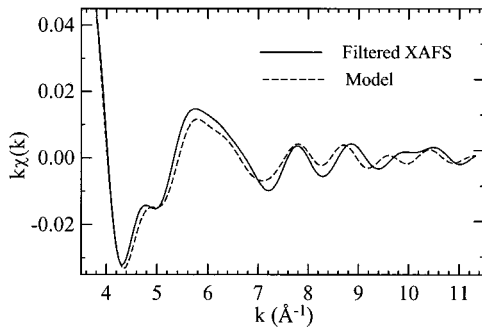


FIG. 4. Comparison of the Fourier-filtered data (solid line) with a model involving Br-[O(4), Ba, Cu(1,2)] pairs (dashed line). Structural parameters extracted from the nonlinear least square-fit are provided in Table I.

O(4), Ba, or Cu(2) and two Cu(1) atoms about Br in the Cu(1) site. This set of coordination numbers implies the cluster is randomly oriented with respect to the polarization vector \mathbf{E} , and, therefore, with respect to the host crystalline structure. The agreement factor for the model is 2.3 times lower than that for the closest competitive model assuming two cells to be combined along the a or b axis of the crystal. The coordination number for CuBr* was found to be 1. Finally, we constrained the energy shifts to values extracted from the previous fit, while allowing the coordination numbers to vary. The best fit is shown by dashed line in Fig. 4. It is in reasonably good agreement with the experimental data. The results are summarized in Table I.

Significantly lower coordination numbers found about the Br atom unambiguously indicate that *Br does not enter the Cu(1) site in the perfect YBCO lattice*. However, good agreement between all four Br-X [$X = \text{O}(4)$, Ba, Cu(1), Cu(2)] interatomic distances obtained from the fit suggests that *Br occupies the Cu(1) site in Br-O(4)-Ba-Cu₂(1)Cu(2)-... nanoclusters (nanofragments)* which yet retain the three-dimensional (3D) structure of the original YBCO lattice. The coordination numbers extracted suggest that those nanoclusters are randomly oriented in the brominated crystal.

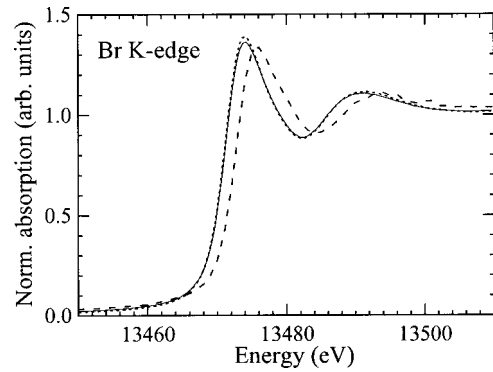


FIG. 5. Polarized Br K -edge XANES spectra of BrYBCO, measured at $\varphi = 45^\circ$ (solid line) and $\varphi = 90^\circ$ (dotted line). Note that no polarization dependence is observed, implying that Br-O(4)-Ba-Cu₂(1)Cu(1)-... nanoclusters are randomly distributed with respect to the x-ray polarization and, therefore, with respect to the host YBCO lattice. Br K -edge XANES of powder BaBr₂·2H₂O (dashed line) shows that the formal Br valence in brominated YBCO is close to -1 .

Independent confirmation for this fact comes from absence of polarization dependence of Br K -edge x-ray-absorption near-edge structure performed on the same brominated crystal at two different experimental geometries (Sec. II): $\varphi = 45^\circ$ and $\varphi = 90^\circ$ ($\mathbf{E} \parallel \mathbf{ab}$). As revealed in Fig. 5, a detailed comparison over the range of 13 440–13 520 eV shows no essential differences between the two spectra. Such a weak polarization dependence is possible if clusters are randomly oriented with respect to the polarization vector \mathbf{E} , and, therefore, with respect to the oriented host crystalline structure.

Considering the uniqueness of the obtained solution, it is worth recalling that the single scattering (SC) fit to XAFS data provides interatomic distances and coordination numbers, but not a 3D picture of the clusters about the absorption site. In turn, this raises a question on the phase composition—is Br-O-Ba-Cu₃-... a well-defined nanophase or is the structure (probed as an average over the bulk) a mixture of simpler nanofragments, like Br-O and Br-Ba with the same in-

TABLE I. Local structural parameters obtained from the constrained fit of the Fourier-filtered Br K -edge $k\chi(k)$ data. S_o^2 was estimated to be 0.72 from the first peak fit. Neutron-diffraction results on YBCO ($y = 0.51$) (Ref. 15) are given for comparison of Cu(1)- X interatomic distances and number of neighbors. Parameters for conventional CuBr powder are taken from Ref. 16. Errors in the parameters were estimated from the covariance matrix generated from the fit and should be taken as relative errors corresponding the reproducibility of the XAFS data.

Br K -edge XAFS				Neutron diffraction		
Bond	R (Å)	No. of neighbors	$\sigma^{(2)} \times 10^3$ (Å ²)	Bond	R (Å)	No. of neighbors
Br-O(4)	1.84 ± 0.02	1.0 ± 0.1	13 ± 2	Cu(1)-O(4)	1.8325	2
Br-Ba	2.51 ± 0.03	1.0 ± 0.2	21 ± 5	Cu(1)-Ba	2.5140	8
Br-Cu(1)	3.89 ± 0.03	2.2 ± 0.4	15 ± 5	Cu(1)-Cu(1)	3.8392	2
					3.8791	2
Br-Cu(2)	4.16 ± 0.04	1.0 ± 0.3	10 ± 3	Cu(1)-Cu(2)	4.1932	2
Br-Cu	2.45 ± 0.04	1.2 ± 0.4	27 ± 9	Br-Cu		4
(in BrCu*)				(in BrCu)		

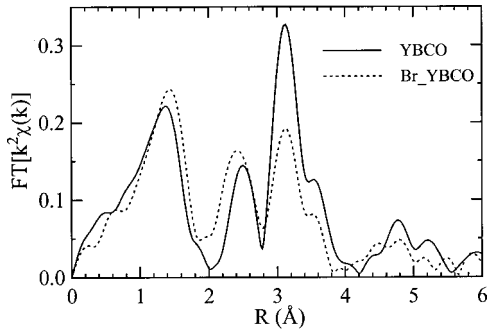


FIG. 6. FT of Cu K -edge $k^2\chi(k)$ of untreated (solid line) and brominated (dashed line) YBCO ($y \sim 0.6$). The data are transformed with a square window between 2.5 and 13.0 \AA^{-1} . The origin of the peaks is described in the text.

teratomic distances and coordination numbers as listed in Table I. Either scenario would be in line with the XAFS refinement. The 3D structure could be accessed either through a detailed analysis of multiple-scattering (MS) terms which are basically small additions to the SC contribution in the strongly distorted compounds or through an analysis of XANES spectra which are dominated by the MS contributions. For the moderate signal-to-noise ratio achieved in Br K -edge XAFS spectra [Fig. 2(a)], the XANES analysis appears to be preferred. Below, we will restrict our discussion to quantitative analysis of normalized Br K -edge XANES spectra shown in Fig. 5, while leaving detail MS simulations to be done in a further work. Bromine in Br-O and Br-Ba nanofragments, if any, would have to have formal valence states of about (+1) and (-2). The position of the main edge depends on formal valence of the absorbing atom, showing an upward shift of the main line position as the formal valence increases. The XANES spectra from two phases with different valence is expected to display additional peaks associated with those valences or, at least, to be broadened compared to XANES spectrum of a single phase characterized by some specific valence state. As seen from Fig. 5, the Br K edge of brominated YBCO does not exhibit additional structures. Comparison with the Br K edge of $\text{BaBr}_2 \cdot 2\text{H}_2\text{O}$ reveals that they are very much alike, indicating the *formal* Br valence in brominated YBCO to be -1, and therefore eliminating the model of mixed Br-O and Br-Ba nanophases as possible products of bromination.

B. c -axis-polarized Cu K -edge EXAFS

The magnitudes of Fourier-transform (FT) spectra of the c -polarized Cu K edge $k^2\chi(k)$ of normal and brominated samples are shown in Fig. 6. The first peak (~ 0.8 – 2.1 \AA) corresponds to Cu(1)-O(4) and Cu(2)-O(4) pairs. A multipole structure (~ 2.3 – 4.2 \AA) is due to combined contributions of Cu(2)-Y, Cu(2)-Cu(2), Cu(1,2)-Ba, Cu(1)-Cu(2), and Cu(2)-O(2,3,4) single-scattering paths as well as several multiple-scattering paths. Since the first peak is well separated, it was isolated through a back FT to k space. A good fit to the $k^2\chi(k)$ filtered data was achieved, revealing Cu(1)-O(4) and Cu(2)-O(4) distances of 1.83 ± 0.01 and $2.33 \pm 0.02 \text{ \AA}$, in good agreement with the results of neutron dif-

fraction for YBCO ($y = 0.51$) single crystals.¹⁵ Results of the fit (including Y, Ba, and Cu environments) are listed in Table II. It is worth mentioning that although there is no obvious beat at $\sim 12 \text{ \AA}^{-1}$ at room temperature, the DW factors for Cu(2)-O(4) and Cu(2)-Cu(2) pairs are abnormally large [2–3 times larger than those for YBCO ($y \sim 0.95$) (Ref. 18) implying that the Cu(1,2)-O(4) and Cu(2)-Cu(2) pair distributions are more complex than a single-site distribution. Apparently, this makes the $y \sim 0.5$ composition a better choice to explore a possible splitting of the O(4) position,^{18,19} and suggests out-of-plane displacements of the Cu(2) atoms.²⁰ A detailed temperature-dependence study is required.

Comparing the FT spectra of the normal and brominated samples we note a very unusual behavior of the first Cu-O peak: it is shifted to higher r with increased intensity, while the Cu-Y, Cu-Cu, and Cu-Ba peaks are reduced, presumably due to structural disorder accompanying the bromination. A detailed analysis of Cu-Y, Cu-Cu, Cu-Ba shells in the framework of a two-phase model (Sec. II) requires a larger number of fit parameters than is allowed by the $\mathbf{E}||c$ data, and, therefore it is not attempted in this work. We will focus on the Cu-O pair correlations. Fits to the filtered Cu-O shells were performed in terms of three constrained models which differ in the number of Cu-O shells. Model 1S uses a single Cu-O bond which is equal to the mean distance the complex Cu-O pair distribution, possibly in a multiphase sample. Model 2S describes the typical YBCO structure in the $\mathbf{E}||c$ geometry: two Cu(1,2)-O(4) distances and corresponding coordination numbers were allowed to vary, while the number of the pairs were fixed to 2. Note that 2S is explicitly a single-phase model. Finally, we considered the 3S model assuming a 2:1 ratio of two phases: one has Cu(1,2)-O(4) pairs typical of the YBCO family, while the other is characterized by an average Cu-O bond length of about 1.95 \AA . The origin of the latter bond will be discussed briefly.

Before proceeding with the fit, we constructed a difference, $k^2[\chi_B(k) - \alpha\chi_N(k)]$, where $\chi_B(k)$ and $\chi_N(k)$ refer to brominated and normal samples, and $\alpha = \frac{2}{3}$. Fits to the first-shell data gave 3.8 ± 0.5 oxygen neighbors at $1.95 \pm 0.01 \text{ \AA}$, with a very small DW factor ($\sim 0.0015 \text{ \AA}$). It is therefore highly unlikely that this peak is composed of several different Cu-O distances. Next, the Cu-O peak of the difference $k^2[\chi_B(k) - \alpha\chi_N(k)]$ was fit as a function of the parameter α . A single-site distribution allowing R , $\sigma^{(2)}$, and ΔE_0 parameters to vary freely, while holding the number of oxygen neighbor to four, was employed. We found that an agreement factor (defined in the caption to Table II) has a flat minimum at $\alpha \sim 0.6$ which validates the ratio 2:1 used in the 3S model.

The best-fit curves corresponding to three models are plotted in Fig. 7 along with the Fourier-filtered contribution from the Cu-O peak. Model S1 (dashed line) gives a poor fit. It does not pass the χ^2 test. Model 2S (dots) demonstrates a good agreement to $k \leq 10 \text{ \AA}^{-1}$, deviating above. The estimated shortest Cu-O distance of 1.91 \AA appears to be unrealistically long for a Cu(1)-O(4) bond in YBCO ($0 < y < 1$). Model S3 (dot-dashed line) provides a fit over whole range, yielding the lowest (among the competing models) reduced agreement factor R_a (Table II). Two observations are

TABLE II. Local structural parameters obtained from the constrained fit of the Fourier-filtered Cu K -edge $k\chi(k)$ data. $S_o^2=0.8$ for all Cu-O bonds and 0.9 for all other bonds. Three models ($S1-S3$) of Cu-O pair distribution are constructed as described in the text. Reduced agreement factor, $R_a=1/(\gamma M)\sum_i^M k(\chi_i^{\text{exp}}-\chi_i^{\text{calc}})$, where M is a number of data points, γ is the number of degrees of freedom in the fit. The $S1$ model does not pass the χ^2 test for the quality of the fit to the filtered data, while both $S2$ and $S3$ do. Neutron-diffraction results on YBCO ($y=0.51$) (Ref. 15) are given for comparison of Cu(1)- X interatomic distances and number of neighbors. *Fixed in the fit.

Sample	Bond	Cu K edge XAFS				Neutron diffraction	
		R (Å)	N	$\sigma^{(2)}\times 10^3$ (Å ²)	$R_a\times 10^3$	R (Å)	N
YBCO ($y=6.6$)	Cu(1)-O(4)	1.83 ± 0.01	2*	3.3 ± 0.4		1.8325	2
	Cu(2)-O(4)	2.33 ± 0.02	2*	18 ± 4		3.3607	2
	Cu(2)-Y	3.21 ± 0.02	4.3 ± 0.4	4.4 ± 0.6		3.2026	4
	Cu(2)-Cu(2)	3.35 ± 0.04	1.1 ± 0.2	24 ± 9		3.3527	1
	Cu(2)-Ba	3.41 ± 0.02	7.8 ± 0.8	4.1 ± 0.5		3.3711	8
	Cu(1)-Ba	3.51 ± 0.03	4.5 ± 0.6	9.2 ± 1.5		3.5140	4
	Cu(2)-Cu(1)	4.19 ± 0.03	4.8 ± 1.0	10.0 ± 2.0		4.1932	4
Br_YBCO 1S model	Cu-O	1.91 ± 0.01	4*	11.6 ± 1.0	6.7		
Br_YBCO 2S model	Cu(1)-O(4)	1.91 ± 0.01	2*	2.2 ± 0.2	4.7		
	Cu(2)-O(4)	2.33 ± 0.02	2*	22 ± 8			
Br_YBCO 3S model	Cu(1)-O(4)	1.85 ± 0.01	4/3*	2.5 ± 0.5			
	Cu(2)-O(4)	2.29 ± 0.02	4/3*	14.3 ± 2.1	3.3		
	Cu(2)-O(2,3)	1.95 ± 0.01	4/3*	1.3 ± 0.3			

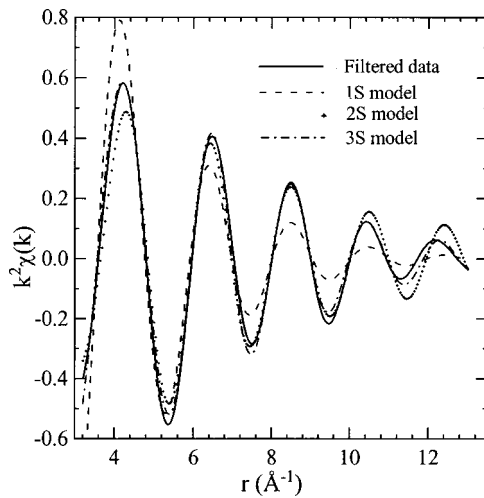


FIG. 7. Comparison of the Fourier-filtered Cu-O contribution to c -axis-polarized $k^2\chi(k)$ with three structural models for the Cu-O pair distribution in BrYBCO. The back FT range is 1–2.1 Å, using a square window. A three-shell model providing the best fit to the filtered data assumes two Cu-O distances resembling Cu(1)-O(4) and Cu(2)-O(4) in optimally doped single-crystal YBCO ($y\sim 0.9-1$) and one more Cu-O distance (of ~ 1.95 Å) due to the decomposed phase. The latter distance is mostly responsible for increase of the Cu-O peak intensity seen in Fig. 6 for the brominated sample.

important in order to understand the mechanism for the restoration of superconductivity in the brominated sample:

(i) Cu(1,2)-O(4) distances and corresponding DW factors associated with the parent YBCO phase are similar to those expected in optimally doped crystals ($y\sim 0.9-1$).¹⁸

(ii) The intermediate Cu-O distance (1.95 ± 0.01 Å) is remarkably similar to the Cu(1)-O(1) Cu(2)-O(2), and Cu(2)-O(3) bond lengths, which for YBCO ($y=0.51$) are equal to 1.928, 1.936, and 1.955 Å, respectively.¹⁵ Note that in the $\mathbf{E}\parallel\mathbf{c}$ geometry there should be no contribution from the above bonds in the Cu-O XAFS, unless these bonds are misaligned with respect to the c axis of the brominated crystal. The Cu-O bonds at a distance of 1.95 Å should be viewed as constituting the secondary (decomposed) phase incorporated by the “host” YBCO lattice.

C. Polarized Cu K -edge XANES

Polarized Cu K edges of normal and brominated YBCO ($y\sim 0.6$) measured for $\mathbf{E}\parallel\mathbf{c}$ and $\mathbf{E}\parallel\mathbf{ab}$ are shown in Fig. 8. To ascertain the dominant trend in the XANES upon bromination we compare our polarized data with those for two oriented powders of YBCO ($y\sim 0.23$ and 1.) reported by Tranquada *et al.*²¹ in their Fig. 2. In the $\mathbf{E}\parallel\mathbf{c}$ geometry the XANES spectra of both brominated YBCO and YBCO ($y\sim 1$) (from Ref. 21) are shifted (nonrigidly) toward low energy by ~ 1.5 eV, compared to spectra of the normal YBCO

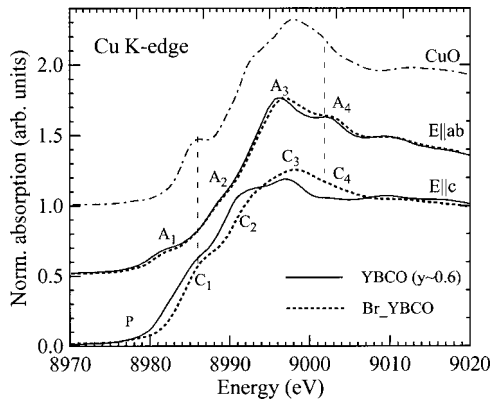


FIG. 8. Effect of bromination on the Cu K -edge XANES of YBCO ($y \sim 0.6$) measured with x-ray polarization vector parallel to the c axis ($\mathbf{E}||c$) and parallel to the ab plane ($\mathbf{E}||ab$). Cu K -edge XANES spectrum of CuO powder (dot-dashed line) and $\mathbf{E}||ab$ spectra are offset for clarity. The solid lines correspond to the pristine sample, while dashed lines are for the brominated crystal. This plot has to be compared to Fig. 2 of Ref. 21 showing the effect of oxygen composition on the Cu K -edge XANES of YBCO, $y = 0.23, 1$.

and YBCO ($y \sim 0.23$) samples. The main feature C_3 decreases, while the C_2 shoulder becomes more pronounced. In the $\mathbf{E}||ab$ geometry, the peak A_1 and, to a smaller extent, the shoulder A_2 , are suppressed as a result of both bromination and the increase of y from 0.23 to 1 in the oriented powder. Such a behavior is in line with the general thought that a reoxygenation of the sample takes place at the expense of decomposition.⁴ Decomposition implies the appearance of additional phases (products of the reaction). A careful inspection of our polarized spectra reveals several differences between brominated and fully oxygenated samples (from Ref. 21). In $\mathbf{E}||c$, the shoulder C_1 is very weak in YBCO ($y \sim 1$) (Ref. 21), while it is very apparent in our brominated sample. One might note that this feature becomes even stronger upon bromination of YBCO ($y \sim 0.6$)—in reverse order to the observed trend upon oxygenation. Bromination gives rise to additional spectral intensity at the A_4 and C_4 features, which are clearly beyond the limits observed as y goes from 0.23 to 1. Finally, $\mathbf{E}||c$ and $\mathbf{E}||ab$ spectra of Br_YBCO are smoother than any spectrum of YBCO (regardless of the oxygen content), implying that the local structure of Br_YBCO is strongly distorted and/or that the sample is composed of different phases.

Interestingly, the above mentioned differences can be satisfactorily understood by assuming that Br_YBCO contains an admixture of a decomposed phase that, in a first approximation, is reminiscent of “CuO powder” shown in Fig. 8 by the dot-dashed line. Difference spectra for 100% Br_YBCO and 66% untreated YBCO ($y \sim 0.6$) were formed for both polarizations. Being normalized to unity in the extended area, they are plotted in Fig. 9 along with the normalized spectra of CuO powder. The $\mathbf{E}||c$ difference is also shifted by -1.3 eV to match the CuO data. The energy positions of all major peaks in the $\mathbf{E}||c$ difference spectrum and the spectrum of the CuO powder almost coincide, although the magnitudes of these peaks are slightly different. The $\mathbf{E}||ab$ dif-

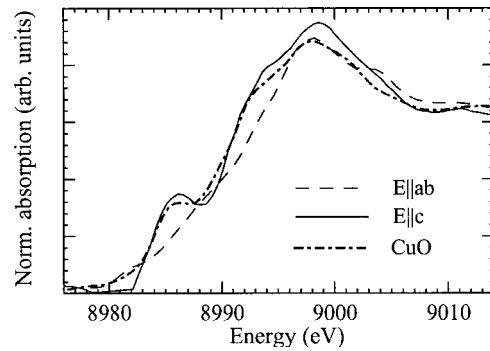


FIG. 9. Contribution to the Cu K -edge XANES from the decomposed phase evaluated as the normalized difference of XANES spectra of BrYBCO and two-thirds that of pristine YBCO vs energy. The polarization dependence represented by solid ($\mathbf{E}||c$) and dashed ($\mathbf{E}||ab$) lines is weak compared to that in single-crystal YBCO, though it is not totally diminished as for the Br K -edge XANES shown in Fig. 5. Residual Cu K -edge polarization dependence implies that domains forming the decomposed phase are *differently ordered* with respect to the x-ray polarization (and, therefore, with respect to the crystal) in opposed to the *random orientation* of Br-O-Ba-Cu₃-... and Br-Cu-... impurity domains. The XANES spectrum of powder CuO is shown by the dot-dashed line for comparison.

ference of the brominated sample retains weak features of the original $\mathbf{E}||ab$ polarized spectrum (A_1 and A_4) which do not match those of the CuO powder. However, their major peaks and oscillations in the extended area ($E > 9010$ eV) coincide reasonably well. Note that the decomposed phase is neither completely amorphous nor is it completely randomly oriented with respect to the major phase. A weak polarization dependence is seen in Fig. 9, presumably due to the different

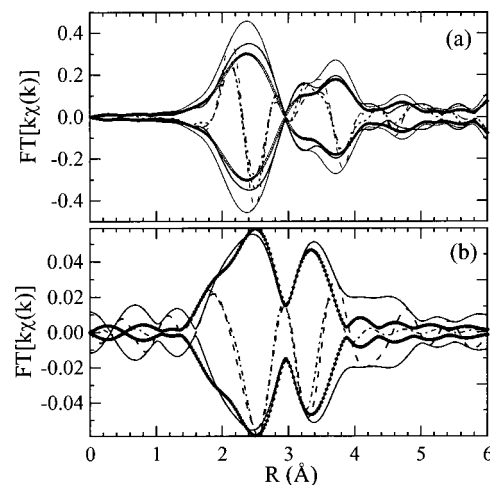


FIG. 10. FT of Ba L_3 -edge $k\chi(k)$ vs k . Panel (a) shows magnitudes and imaginary parts of pristine and brominated crystals: (thin solid and thin dashed lines) and (solid and short dashed lines) as well as the pristine sample scaled to two-thirds of its original values (dot and dot-dashed lines). The FT range is $1.8\text{--}9 \text{ \AA}^{-1}$ with a square window. Panel (b) illustrates a fit to the FT of $k\chi(k)$ performed in the r space for $1.7\text{--}3.7 \text{ \AA}$. The constrained fit includes Ba-O, -Cu(1,2), -Y, and Ba-Ba shells.

TABLE III. Results of Ba L_3 -edge XAFS analysis of the decomposed phase. $S_o^2=0.95$. Errors in numbers of Ba neighbor are below 25%. The constrained parameters are taken from neutron-diffraction results on YBCO ($y=0.51$) (Ref. 15). The loss of the XAFS signal in the medium-to-long range pair correlations ($R>4 \text{ \AA}$) is probably due to cancellations of these contributions in the aperiodic media.*Fixed in the fit.

Sample	Bond	$R \text{ (\AA)}$	$\sigma^{(2)} \text{ (\AA}^2\text{)}$	N
	Ba-O	2.82	0.029	8
	Ba-Cu(2)	3.40	0.005	4*
$k\chi(k)$ difference	Ba-Cu(1)	3.51	0.008	2
Br_YBCO-0.66*YBCO	Ba-Y	3.80*	0.003	1*
	Ba-Ba	3.85*	0.003	2*

orientations of decomposed domains with respect to the host lattice.

D. Ba L_3 -edge XAFS

Magnitudes and imaginary parts of the Fourier-transformed $k\chi(k)$ spectra of normal and brominated crystals are shown in Fig. 10(a). In untreated YBCO the first peak corresponds to three Ba-O groups at 2.74, 2.87, and 2.98 \AA .¹⁵ The second double-peak structure is dominated by Ba-Cu(1,2), Ba-Y, and Ba-Ba contributions. The peak heights for brominated sample are reduced. In the same plot the magnitudes and imaginary parts of normal YBCO are scaled to two-thirds of their original value. For $R>3.5 \text{ \AA}$ the spectra are almost identical to those of the brominated sample. To analyze the local structure of the decomposed phase, the difference of the 100% brominated signal and 66% of the as-prepared YBCO ($y\sim 0.5$) was computed. We will ignore the interference between the $p\rightarrow d$ and $p\rightarrow s$ channels in Ba L_3 -edge XAFS, since the decomposed phase shows a weak polarization dependence (see Sec. III C), and the contribution of the $p\rightarrow s$ channel is significantly weaker than that of the $p\rightarrow d$ channel. The Fourier transform of the resultant $k\chi(k)$ spectrum consists of two peaks, which are assigned to Ba-O and Ba-Cu, Ba-Y, and Ba-Ba bonds [Fig. 10(b)]. Because of the short available range in the k space, a single-distance Ba-O distribution was considered. The best fit is shown in Fig. 10(b). Extracted parameters are summarized in Table III.

The local structure of the decomposed phase with respect to the Ba site is given by a cluster expansion Ba-O₈-Cu(2)₄Cu(1)₂-YBa₂-... Importantly, only two of four Ba-Cu(1) bonds [which are only $\sim 0.1 \text{ \AA}$ longer than the Ba-Cu(2) bonds] were observed in the fit. This is consistent with Br K -edge data, implying the homogeneity of the Cu(1)-O(1) planes as Br is substituted into the Cu(1) position of the fragmented lattice (see Sec. III A) and with the Cu K -edge XANES results, as we shall discuss in Sect. IV.

E. Y K -edge XAFS

The Fourier-transformed $k\chi(k)$ data of normal and brominated sample are compared in Fig. 11. The first three

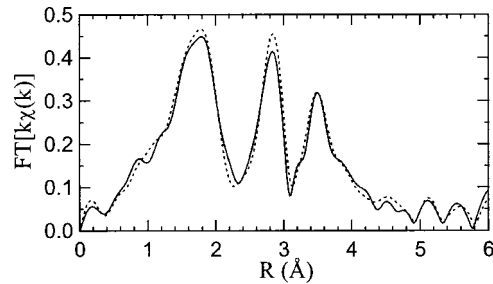


FIG. 11. FT of Y K -edge $k\chi(k)$ of untreated (solid line) and brominated (dashed line) YBCO ($y\sim 0.6$). The data are transformed with a square window between 1.9 and 14.7 \AA^{-1} .

peaks correspond to Y-O(2,3), Y-Cu(2), and Y-Y pairs. In contrast to Cu K and Ba L_3 edges, Y K -edge data exhibit only minor changes upon bromination. Structural parameters for the oxygen and copper shells of normal and brominated sample are summarized in Table IV. Since the changes are small, an application of the two-phase model used in the previous sections is not obvious. Therefore fits were performed to the Y K -edge data of Br YBCO and YBCO corresponding to single-phase and two-phase models. This implies that the local distortions in Y-O(2,3) and Y-Cu(2) pairs are homogeneously distributed throughout the sample. The latter associates the local distortions with the decomposed phase, while the major phase remains undistorted. Following the previous results, the mixture of major and distorted phase was fixed at 2:1. All atomic parameters for the undistorted phase were further constrained as determined from our XAFS fit of normal YBCO ($y\sim 0.6$). Both models gave very similar agreement factors. Therefore, the data are consistent with either model. Y-O(2,3) and Y-Cu(2) distances and oxygen and copper coordination numbers remain the same within the resolution of our experiment and are consistent with the diffraction results (Table IV). The only parameters to differ in the models are the DW factors, which are slightly larger in the distorted phase. As will be shown in Sec. IV, a combined analysis of the Cu K -, Ba L_3 and Y- K edge data requires a mixture of two phases. *However, regardless of the model used for the Y K -edge data, the extracted structural parameters provides clear evidence that the local structure of the superconducting Cu(2)-O(2,3)₂ planes is not affected by bromination.*

IV. DISCUSSION

Previous scanning electron microscopy and EDAX measurements on YBCO ceramic addressed the macroscopic and chemical homogeneity at scales of several hundred \AA and larger.²² Br treatment of YBCO increases the grain size and porosity. Larger grains are elongated along certain directions, but they do not precipitate secondary phases and have the same chemical composition as untreated YBCO. In our attempt to address the chemical composition on an atomic scale, we rely on a multiple-edge XAFS analysis.

As shown in Secs. III B-III D, the local structure of the distorted phase about Cu, Ba, and Y sites can be expressed as the cluster expansions: Cu(1,2)-O₄-..., Ba-O₈

TABLE IV. Local structural parameters for the oxygen and copper shells about the yttrium in normal and brominated YBCO ($y \sim 0.6$). Parameters are derived from the nonlinear least-square fit to the Fourier filtered $k\chi(k)$ data. Back FT ranges were 1.4–2.2 and 2.3–3.1 Å, respectively. From the fit of normal YBCO the S_o^2 was estimated to be 0.9, and was fixed in the refinement of Br_YBCO. Only parameters referring to the distorted (decomposed) phase are listed for the two-phase model, since the parameters for the undistorted phase were constrained to those in normal YBCO (first two rows in this table). Neutron-diffraction results on YBCO ($y=0.51$) (Ref. 15) are given for comparison.

Sample	Bond	Y <i>K</i> -edge XAFS			Neutron diffraction	
		R (Å)	N	$\sigma^{(2)} \times 10^3$ (Å ²)	R (Å)	N
Normal	Y-O(2,3)	2.39 ± 0.01	8.2 ± 1	4.1 ± 0.5	2.3922/2.4082	4/4
YBCO ($y \sim 0.6$)	Y-Cu(2)	3.22 ± 0.01	7.8 ± 1	4.4 ± 0.4	3.2026	8
Br_YBCO (single phase)	Y-O(2,3)	2.39 ± 0.01	7.9 ± 1	4.3 ± 0.5		
	Y-Cu(2)	3.22 ± 0.01	8.0 ± 1	4.9 ± 0.6		
Br_YBCO distorted phase	Y-O(2,3)	2.40 ± 0.01	2.4 ± 0.3	5.8 ± 0.7		
	Y-Cu(2)	3.21 ± 0.01	2.7 ± 0.3	5.4 ± 0.7		

-Cu(2)₄Cu(1)₂-..., and Y-O(2,3)₈-Cu(2)₈-... Corresponding expansions of the single-phase YBa₂Cu₃O_{6+y} are Cu(1,2)-O(2,3,4)₄O(1)_{2/3*y}-..., Ba-O(4)₄-Cu(2)₈Cu(1)₄-..., and Y-O(2,3)₈-Cu(2)₈-... The difference in local chemical compositions [in O(1) and Cu(1) stoichiometries] about Cu(1) and Ba sites affirms that a decomposition reaction does take place. The decomposed phase is not YBCO with $0 < y < 1$. Ba-, Y-, and Cu-oxides (BaO, Y₂O₃, Cu₂O, and CuO) or barium cuprates (BaCuO₂, Ba₂CuO₃,...) are often seen in the literature as likely components of the decomposed phase. However, even if they are considered in the form of nanoparticles (with typical sizes of ~ 10 – 20 Å and larger)—and therefore do not scatter elastically—they cannot provide all three components listed above. For instance, Y₂O₃ oxide has an oxygen shell about the Y similar to YBCO, but does not have Y-Cu pairs. In both BaO and YBCO, the Ba atom is fourth oxygen (4) coordinated. Ba-O distances are very much alike in these compounds. However, an assumption on BaO oxide cannot explain observation of Ba-Cu pairs revealed by Ba *L*₃-edge XAFS. The presence of Y-Cu and Ba-Cu pairs causes the decomposed phase to differ from that of CuO oxide. Before we construct a pictorial view of brominated YBCO we would like to make four points:

(i) Oxygenation of the pristine YBCO phase takes place at the expense of deoxygenation of the decomposed phase. Indeed, the bromination in the nitrogen atmosphere employed in this work excludes external oxygenation. A chemical balance implies that, if oxygenation of one of the phases takes place, then at least that amount of oxygen had to defuse from the other decomposed region. In YBCO ($y \sim 0.6$) the most likely candidates for diffusion are O(1) atoms which are well known to be quite mobile at $T = 260$ °C (the temperature of bromination). The current multiple-edge analysis provides supporting evidence for O(1) diffusion from the decomposed to superconducting phase: the Y *K*-edge XAFS data (Sec. III E) revealed that the local structure of CuO₂ planes composed of Cu(2)-O(2,3) atoms is preserved. Cu-O coordination numbers extracted from the Cu *K*-edge XAFS fit (Sec.

III B) requires a nonzero oxygen coordination about the Cu(1) site. (Otherwise, the total coordination number about Cu falls beyond the estimated error bar.) The Ba *L*₃-edge XAFS analysis (Sec. III D) confirms Cu *K*-edge data showing Ba to be fourfold oxygen coordinated. Thus Y-edge XAFS imply that O(2,3) sites are heavily populated, while Cu *K*- and Ba *L*₃-edge XAFS analyses ensure that O(4) sites are populated as well. Therefore, by exclusion, among all oxygen sites in the decomposed phase only the O(1) occupancy is altered. The nature of the changes in Cu *K*-edge XANES (Sec. III C) suggests an increase of overall oxygen concentration in the well-ordered phase due to the population of vacancies in O(1) sites. The same is evidenced by Cu *K*-edge XAFS analysis of the Cu-O pair distribution along the *c* axis. It is well known from the diffraction measurements that the difference between Cu(2)-O(4) and Cu(1)-O(4) distances decreases from 0.42 to 0.33 Å as y increases from 0.5 to 0.95.¹⁵ The trend is clearly seen from Cu *K*-edge XAFS results (Table II) as one goes from pristine to brominated crystals.

(ii) There might be a mechanism disfavoring the formation of macroscopic decomposition. As we know from the literature,²³ the concentration of Br in the underdoped samples is much larger than in oxygen-rich YBCO (for the same condition of bromination). We suggest that Br locally decomposes YBCO ($y \sim 0.6$) and liberates O(1) atoms which enter empty neighboring O(1) sites driving the local oxygen content to the optimal level, and, thereby, preventing a new nucleus of the decomposed phase from being created nearby.

(iii) A combined analysis of the three cluster expansions about Y, Ba, and Cu sites shows that the decomposed phase consists of nanofragments of YBCO. Cu *K*-edge polarization-dependent measurements indicate the nanofragments to be misoriented with respect to the host lattice.

(iv) Cu *K*-edge XANES data imply that the local structure of YBCO nanofragments forming the decomposed phase is broken about the Cu(1)-O(1) planes. In a perfect YBCO structure both Cu(1) and Cu(2) sites contribute to the total x-ray absorption cross section, providing one-third and two-

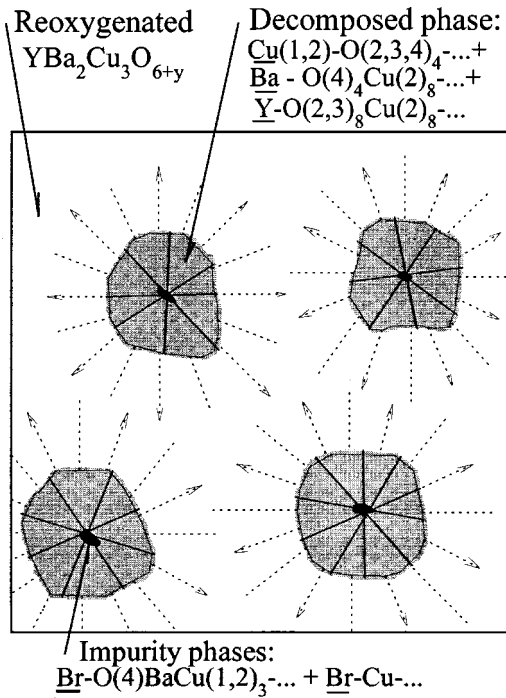


FIG. 12. Polarized Cu K -, Y K -, Ba L_3 -, and Br K -edge measurements are consistent with nanoscale heterogeneity in brominated YBCO ($y \sim 0.6$). Well-ordered, undistorted YBCO lattice hosts differently ordered and heavily distorted decomposed inclusions (gray regions) which accounts for about one-third of the volume. The decomposed phase consists of nanofragments (nanodomains) formed as a result of truncation of the YBCO lattice predominantly along the Cu(1)-O(1) planes accompanied by the fragment rearrangement with respect to the host lattice. The typical size of the decomposed areas is unknown, but is expected to be no less than 7–8 Å, since Br enters the Cu(1) site forming impurity phases (small black regions inside the gray ones) and causing at least eight unit cells to decompose. The local structure of the host lattice coincides with that of oxygen-rich YBCO ($y \sim 0.9-1$) (Ref. 18), presumably due to reoxygenation of the pristine YBCO ($y \sim 0.6$) by O(1) diffusing from the decomposed regions. The local structure of the decomposed and impurity phases is expressed in terms of cluster expansions undertaken about Cu, Ba, Y, and Br absorption sites (underlined). The interatomic distances and Debye-Waller parameters are provided in the text.

thirds of the total signal, respectively. Differential XANES spectra are similar to CuO oxide (Fig. 9), i.e., the major signal comes from the Cu(2) sites while the contribution from Cu(1) sites is effectively diminished. This condition is met if local environment about Cu(1) is strongly disturbed. With respect to (i), losses of O(1) atoms which are the nearest neighbors of Cu(1) are not sufficient—the differential spectra have little resemblance to Cu K -edge XANES of YBCO ($y \sim 0$) powder. Results of MS simulations performed for a cluster of 42 atoms about the Cu(1) site shows that the strongest suppression is achieved when the cluster is fragmented rather than just locally distorted from the perfect YBCO structure. It is due to fragmentation that the original coordination is altered for all Cu(1)-X ($X = \text{O, Ba, Y, } \dots$), dramatically reducing the degeneracy of the MS paths. The discontinuation along the Cu(1)-O(1) planes is further sup-

ported by the Ba L_3 -edge XAFS analysis, suggesting a smaller number of Ba-Cu(1) pairs than in YBCO.

Using this information we propose a structural model of a brominated sample depicted in Fig. 12. In terms of a two-component model about one-third of the YBCO lattice is locally decomposed but is incorporated into a well-ordered “host” lattice as a nanoscale second phase. The decomposed phase consists of heavily distorted domains that are differently oriented with respect to the “host” lattice. Structurally, these domains are fragments of the YBCO lattice that are discontinued along the Cu(1)-O(1) planes. This picture implies that YBCO ($y \sim 0.6$) subjected to bromination becomes strongly heterogeneous on atomic length scales. The heterogeneity of brominated YBCO brings about unusual structural and electronic properties. We shall briefly discuss the implications on conventional diffraction, magnetization, and transport measurements.

It is well established that diffraction peaks broaden significantly when bromine is introduced. The broadening, however, should not be directly associated with lattice distortions. In the two-phase model adopted in this paper, the distorted domains do not form any well-defined macroscopic phase. Therefore, they do not scatter elastically and do not give rise to additional diffraction peaks. As for the major phase (hosting the distorted domain inclusions) these inclusions deflect a lattice function in the reciprocal space: $L(r) = \sum_{n_1, n_2, n_3 = -\infty}^{\infty} \delta(r + n_1 a + n_2 b + n_3 c)$. In heterogeneous compounds like Br-YBCO, the sums run over discrete domains of varying sizes, Γ , resulting in the δ -functional profiles to be substituted by Gaussian ones: $L'(r, \Gamma) = \sum_{n_1, n_2, n_3 \in \Gamma} \delta(r + n_1 a + n_2 b + n_3 c)$. The DW factors extracted from a Rietveld refinement will overestimate lattice distortions in the major phase. The weight of the major phase scattering elastically will depend on the coherence length of an x-ray source and does not necessarily coincide with the XAFS estimate ($\sim \frac{2}{3}$ of the pristine sample for $y \sim 0.6$). At the same time, lattice parameters are expected to be less affected by the heterogeneity. Their variation is a reasonable measure of *average* changes in orthorhombicity, volume of unit cell, and oxygen content associated with the major phase. Previous diffraction results found that bromination converts the lattice of underdoped YBCO from tetragonal to orthorhombic phase, with the c parameter reduced: both are signatures of the reoxygenation.

Local structural inhomogeneity could account for the broad superconducting transition seen for the brominated sample. It is instructive to compare the fractional amount of the superconducting phases (Meissner fraction) in the brominated and reoxygenated samples ($y \sim 0.9-1$) if the same YBCO ($y \sim 0.6$) is subjected to either the bromination or reoxygenation. Since we do not have our own data on reoxygenated crystals, the zero-field-cooled magnetization data on 1- μm YBCO powder ($y = 0.6$) shown in Fig. 2 of Ref. 9 will be examined here. Considering a ratio of the residual magnetizations at 10 K, one can estimate that the Meissner fraction in the brominated ceramic is about 60–65% of that in the re-oxygenated powder. Recalling that $\sim \frac{1}{3}$ of brominated crystal is locally decomposed, we speculate that the decomposed phase is not superconducting. The discontinuous be-

havior of the structure and large local distortions are consistent with the observation²⁴ that the room-temperature resistivity of brominated YBCO is ~ 35 times that of normal YBCO with the same critical temperature.

Finally, we would like to point out that the heterogeneity in Br_YBCO ($y \sim 0.6$) differs in its origin from that observed in many high-temperature superconductors²⁵ at low temperatures. In the latter compounds, the nanoscale heterogeneity (or phase separation) is derived from a correlated behavior of the electronic system coupled with lattice degrees of freedom. Though Br_YBCO contains oxygen-rich domains where the above mechanism could be involved, the major factor determining the inhomogeneity is aperiodic and incommensurate arrangements of nanofragments caused by the decomposition reaction.

V. CONCLUSIONS

We have reported on Br *K*-, Cu *K*-, Ba *L*₃-, and Y *K*-edge XAFS measurements of brominated YBa₂Cu₃O_{6+y} crystal (Br/Cu $\sim 1/30$, $y \sim 0.6$) showing a superconducting transition at ~ 89 K. Br *K*-edge data reveal that Br does not enter substitutionally or interstitially into the *perfect* YBCO lattice. Nor does it create a large amount of *amorphous* decomposition products. The major result of this paper is that the brominated sample becomes strongly heterogeneous on atomic length scales.

The heterogeneity can be satisfactorily understood in terms of major and impurity phases. The major phases are well ordered, undistorted, and reoxygenated YBCO lattices, hosting differently ordered and heavily distorted decomposed inclusions, which accounts for about one-third of the sample. The decomposed inclusions comprised of nanofragments (nanodomains) formed as a result of a truncation of the parent YBCO lattice predominantly along the Cu(1)-O(1) planes accompanied by the fragments' rearrangement. Despite the discontinuous behavior there are still highly correlated atom pairs, so that the local structure still can be expressed by cluster expansions. Y-O(2,3)₈-Cu(2)₈..., Ba-O₈Cu(2)₄Cu(1)₂... and Cu-O₄... with respect to Y, Ba, and Cu sites. The typical size of the decomposed domains is unknown, but is expected to be no less than 7–8 Å. Impurity phases ($\sim 1\%$ of the total weight of the sample) are due to Br entering the Cu(1) site of a YBCO *fragment*, forming

Br-O(4)-Ba-Cu₂(1)Cu(2)-... and Br-Cu-... nanoclusters.

An artificial inhomogeneity might partly account for the divergence in the accumulated experimental data,^{1–9} demonstrating that measured physical properties essentially depend on the probing length of the chosen experimental technique. The small size of decomposed and impurity domains prevent them from diffracting elastically. Their presence, however, is observable by local structure-sensitive measurements. Taking advantage of polarization-dependent measurements in FY mode (Sec. III A), we have found that Br is incorporated into randomly ordered nanoclusters which have more complex structure than BaBr₂ considered in Refs. 6 and 9. It is worth mentioning that the Br-Ba interatomic distance in the Br-O(4)-Ba-Cu₂(1)Cu(2)-... cluster is close to the average Br-Ba distance in powder BaBr₂. In addition, Ba is a first heavy element coupled with Br so that x-ray photoemission and Br NMR spectra are expected to be reminiscent of, although not identical to, those of powder BaBr₂. Further theoretical calculations of x-ray-photoemission and NMR spectra of different Br-based nanoclusters will be needed to reconcile remaining differences among the local structural probes.

This present work shows very clearly that bromination of YBa₂Cu₃O_{6.6} crystal must not be considered as doping, since Br atoms destroy the homogeneity of the sample. Br-based nanoclusters are located in the decomposed regions (Fig. 12), which are highly resistive at room temperature²⁴ and apparently are not superconducting (Sec. IV). A direct doping of the CuO₂ planes, therefore, is unlikely. In agreement with previous work,^{4,9} the recovery of superconductivity is attributed to an increase of the oxygen population at the O(1) positions of the well-ordered crystalline phase that is evidenced by (i) the behavior of Cu(1)-O(4) and Cu(2)-O(4) interatomic distances and corresponding DW factors (Sec. III B), and (ii) the nature of the changes in polarized Cu *K*-edge XANES (Sec. III C).

ACKNOWLEDGMENTS

Data acquisition was performed at Brookhaven National Laboratory's National Synchrotron Light Source, which is funded by the U.S. Department of Energy. This work was supported by National Science Foundation Career Grant No. DMR-9733862.

¹(a) Yu. A. Ossipyan, O. V. Zharikov, N. S. Sidorov, V. I. Kulakov, D. N. Mogilyanskii, R. K. Nikoloev, V. Sh. Shekhtman, O. A. Volegova, and I. M. Romanenko, *Pis'ma Zh. Eksp. Teor. Fiz.* **48**, 225 (1988) [*JETP Lett.* **48**, 246 (1988)]; (b) Yu. A. Ossipyan, and O. V. Zharikov, *Physica C* **162–164**, 79 (1989).

²H. B. Radousky, R. S. Glass, P. A. Hahn, M. J. Fluss, R. G. Meisenheimer, B. P. Bonner, C. I. Mertzbacher, E. M. Larson, K. D. McKeegan, J. C. O'Brien, J. L. Peng, R. N. Shelton, and K. F. McCarty, *Phys. Rev. B* **41**, 11 140 (1990).

³M. Mokhtari, C. Perrin, M. Sergent, E. Furet, J. F. Halet, J. Y. Saillard, E. Ressouche, and P. Burllet, *Solid State Commun.* **93**,

487 (1995).

⁴Yu. A. Ossipyan, O. V. Zharikov, V. L. Matukhin, and V. N. Anashkin, *Z. Naturforsch. Teil A* **47**, 21 (1992); M. Mokhtari, O. Peña, A. Perrin, and M. Sergent, *Mater. Lett.* **13**, 241 (1992); D. M. Potrepka, M. Balasubramanian, D. B. Fenner, W. A. Hines, and J. I. Budnick, *Appl. Phys. Lett.* **73**, 1137 (1998).

⁵All atomic sites are labeled following J. D. Jorgensen, M. A. Beno, D. G. Hinks, L. Soderholm, K. J. Volin, R. L. Hitterman, J. D. Grace, I. K. Schuller, C. U. Segre, K. Zhang, and M. S. Kleefisch, *Phys. Rev. B* **36**, 3608 (1987).

⁶Y. Fukuda, N. Sanada, Y. Suzuki, T. Goto, M. Nagoshi, Y. Syono,

- and M. Tachiki, *Phys. Rev. B* **47**, 418 (1993).
- ⁷M. Mokhtari, C. Perrin, M. Sergent, E. Furet, J. F. Halet, J. Y. Saillard, E. Ressouche, and P. Burllet, *Solid State Commun.* **93**, 487 (1995).
- ⁸A. P. Nemudry, Yu. T. Pavlyukhin, N. G. Khainovsky, and V. V. Boldyrev, *Supercond. Rev.* **3**, 1215 (1990).
- ⁹D. M. Potrepka, J. I. Budnick, D. B. Fenner, W. A. Hines, M. Balasubramanian, and A. R. Moodenbaugh, *Phys. Rev. B* **60**, 10 489 (1999).
- ¹⁰T. M. Hayes and J. B. Boyce, in *Solid State Physics*, edited by H. Ehrenreich, F. Seitz, and D. Turnbull (Academic, New York, 1982), Vol. 37, p. 173.
- ¹¹L. Tröger, D. Arvanitis, K. Barberschke, H. Michaelis, U. Grimm, and E. Zschech, *Phys. Rev. B* **46**, 3283 (1992).
- ¹²http://www-cxro.lbl.gov/optical_constants/pert_form.html
- ¹³E. A. Stern, *Phys. Rev. B* **48**, 9825 (1993).
- ¹⁴S. I. Zabinsky, J. J. Rehr, A. Ankudinov, R. C. Albers, and M. J. Eller, *Phys. Rev. B* **52**, 2995 (1995).
- ¹⁵H. Casalta, P. Schleger, P. Harris, B. Lebech, N. H. Andersen, Ruixing Liang, P. Dosanjh, and W. N. Hardy, *Physica C* **258**, 321 (1996).
- ¹⁶S. A. Hodorowicz, E. K. Hodorowicz, and H. A. Eick, *J. Solid State Chem.* **48**, 351 (1983).
- ¹⁷Note that at this point of refinement, the number of fitting parameters does not allow inclusion of even a few multiple-scattering paths. In addition, as will be apparent from further analysis, the local structure about Br is strongly distorted, reducing the effects of multiple scattering.
- ¹⁸C. H. Booth, F. Bridges, J. B. Boyce, T. Claeson, B. M. Lairson, R. Liang, and D. A. Bonn, *Phys. Rev. B* **54**, 9542 (1996).
- ¹⁹J. Mustre de Leon, S. D. Conradson, I. Batistic, A. R. Bishop, I. D. Raistrick, M. C. Aronson, and F. H. Garzon, *Phys. Rev. B* **45**, 2447 (1992); E. A. Stern, M. Qian, Y. Yacoby, S. M. Heald, and H. Maeda, *Physica C* **209**, 331 (1993).
- ²⁰J. D. Sullivan, P. Bordet, M. Marezio, K. Takenaka, and S. Uchida, *Phys. Rev. B* **48**, 10 638 (1993).
- ²¹J. M. Tranquada, S. M. Heald, A. R. Moodenbaugh, and Y. Xu, *Phys. Rev. B* **38**, 8893 (1988).
- ²²S. M. Mukhopadhyay, R. Garcia, and N. Mahadev, *Physica C* **313**, 205 (1999).
- ²³M. Mokhtari, C. Perrin, O. Péna, A. Perrin, and M. Sergent, *Mater. Lett.* **13**, 241 (1992).
- ²⁴P. P. Nguyen, Z. H. Wang, A. M. Rao, M. S. Dresselhaus, J. S. Moodera, G. Dresselhaus, H. B. Radousky, R. S. Glass, and J. Z. Liu, *Phys. Rev. B* **48**, 1148 (1993).
- ²⁵See, for example, T. Egami and S. J. L. Billinge in *Physical Properties of High Temperature Superconductors*, edited by D. M. Ginsberg (World Scientific, Singapore, 1997), Vol. 5.